**Astronomy**
**&**
**Astrophysics**

# The Trumpler 14 photodissociation region in the Carina Nebula

K. J. Brooks[1,2], P. Cox[3], N. Schneider[4], J. W. V. Storey[5], A. Poglitsch[6], N. Geis[6], and L. Bronfman[1]

[1] Departamento de Astronomía, Universidad de Chile, Casilla 36-D, Santiago, Chile
[2] European Southern Observatory, Casilla 19001 Santiago, Chile
[3] Institut d'Astrophysique Spatiale, Université de Paris-Sud, 91405 Orsay Cedex, France
[4] Observatoire de Bordeaux, Université de Bordeaux I, 33270 Floirac Cedex, France
[5] School of Physics, University of New South Wales, Sydney 2052, NSW, Australia
[6] Max Planck für Extraterrestrische Physik, Garching bei München, Germany

**Abstract.** We report the results of observations of the fine-structure emission lines [C II] 158 $\mu$m and [O I] 63 $\mu$m using FIFI on the Kuiper Airborne Observatory (KAO) and the Long Wavelength Spectrometer (LWS) on board ISO, towards the molecular cloud associated with the stellar cluster Trumpler 14 (Tr 14) in the Carina Nebula. These data are compared with selected CO and CS transitions obtained with the SEST as well as IRAS and *MSX* images to produce a detailed view of the morphology and the physical conditions prevailing in the photodissociation region (PDR) at the interface between the ionized gas and the molecular dust lane. The relative intensity distribution observed for the various tracers is consistent with the stratification expected for a molecular cloud seen edge-on and exposed to a radiation field of $\approx 10^4 \, G_0$, which is dominated by the most massive stars of Tr 14. The grain photoelectric heating efficiency, $\epsilon$, is estimated to be $\approx 5 \times 10^{-3}$ and is comparable to other galactic PDRs. The molecular gas has a complicated velocity structure with a high velocity dispersion resulting from the impact of the stellar winds arising from Tr 14. There is evidence of small-scale clumping with a very low volume filling factor. Despite the rich concentration of massive O stars in Tr 14 we find that the parameters of the PDR are much less-extreme than those of the Orion and M 17 massive star-forming regions.

**Key words.** stars: formation – ISM: lines and bands – ISM: clouds – ISM: individual objects: Carina nebula

## 1. Introduction

Throughout their lifetime massive stars (O and B stars) have a dramatic impact on the interstellar medium of galaxies. Starting from birth, their extreme-ultraviolet photons ($h\nu > 13.6$ eV) ionize the surrounding molecular gas forming H II regions. Furthermore, their far-ultraviolet (FUV) photons (6 eV $< h\nu < 13.6$ eV) penetrate beyond the H II region and into the molecular cloud where they dominate the heating and chemistry, giving rise to photodissociation regions (PDRs). PDRs are found to be ubiquitous in star-forming giant molecular clouds (GMCs) (see review by Hollenbach & Tielens 1997 and references therein). Understanding the nature of the interaction between FUV radiation and molecular gas and how it influences the evolution of the cloud is important, particularly with regards to the cloud's star-forming capacity.

Previous studies of galactic massive star-forming regions such as Orion and M 17 (Meixner et al. 1992; Wolfire et al. 1990) infer that the FUV fields in the PDRs associated with these regions are very high ($10^4$–$10^5 \, G_0$, where $G_0 = 1.6 \times 10^{-3}$ erg s$^{-1}$ cm$^{-2}$ is the average intensity of the local Galactic

FUV flux, Habing 1968). In these well-studied cases the brightest stellar members of the exciting cluster are, at most, a few O-type stars. Even the Orion Nebula, which represents the nearest example of a massive-star forming region, is excited by a cluster whose principle members are an O6 and an O9 star (Hillenbrand 1997). To date, there have been no comprehensive PDR studies of galactic regions harboring higher concentrations of O-type stars. Results from PDR studies towards the massive stellar cluster R136 in the 30 Doradus Nebula (30 Dor) of the Large Magellanic Cloud (which contains more than 30 O3 stars, Walborn & Blades 1997), are consistent with a significantly lower incident FUV field ($10^2$–$10^3 \, G_0$, Israel et al. 1996) than regions like Orion and M 17. A lower FUV field is rather surprising given the extreme stellar radiation field the molecular gas would be exposed to. Not enough is known about the nature of PDRs associated with similarly massive stellar clusters in our galaxy to attribute the lower FUV fields to metallicity effects alone. Perhaps the measured lower FUV field reflects the environment of a more evolved star-forming region in which the molecular gas in the immediate vicinity of the massive cluster has been destroyed.

The Carina Nebula is renowned for its rich concentration of massive stars and is often likened to 30 Dor in that

---

*Send offprint requests to*: K. J. Brooks,
e-mail: kbrooks@das.uchile.cl

respect. The two most influential star clusters associated with the Carina Nebula are Trumpler 14 and Trumpler 16 (hereafter Tr 14 and Tr 16) which contain a combined total of more than 30 O stars, including several O3 stars (Feinstein 1995; Vázquez et al. 1996). Tr 16 also harbors one of the most massive stars known – Eta Carinae (hereafter $\eta$ Car). Distances to Tr 14 and Tr 16 are quoted in the range 2.2−2.8 kpc (e.g. Davidson & Humphreys 1997), and we will adopt throughout this paper a distance of 2.2 kpc. The relative proximity of such a rich concentration of massive stars makes the Carina Nebula an ideal target for which to study in detail the parameters of both the PDR and the FUV radiation field and see how they compare with 30 Dor and other galactic PDRs.

Figure 1 shows an H$\alpha$ image of the central part of the Carina Nebula. The image is bisected by a prominent optical dark lane that consists of intermixed warm dust and molecular gas situated close to the nebula (Dickel 1974). This dark lane forms the western part of a GMC that extends over 150 pc (Grabelsky et al. 1988). Prevalent throughout the GMC is CO(4–3) and [C I] emission arising from PDRs, indicating the vast extent to which the FUV radiation field has penetrated into the molecular material (Zhang et al. 2001). All that remains of the GMC in the vicinity of Tr 16 are small externally heated globules (Brooks et al. 2000; Cox & Bronfman 1995). In contrast, the molecular cloud surrounding Tr 14 appears relatively intact, albeit exposed to the effects of strong ionizing radiation and stellar winds of the O3 stars.

In this paper, we present the first comprehensive study of the PDR in the vicinity of Tr 14. We have incorporated a series of molecular-line data at millimetre wavelengths to characterize the properties of the molecular gas. Furthermore we have included data on the far-infrared fine structure emission lines of [C II] and [O I]. These emission lines are dominant gas cooling lines for PDRs and their relative strengths can be used in conjunction with PDR models to constrain the incident FUV radiation field and density of the irradiated gas. All of the observations were centered on the 60 $\mu$m emission peak arising from the dust lane adjacent to Tr 14 (see Fig. 1).

## 2. Observations

### 2.1. KAO observations

The [O I] $^3P_1-^3P_2$ 63.2 $\mu$m and [C II] $^3P_{3/2}-^3P_{1/2}$ 158 $\mu$m maps were obtained with the MPE/UCB Far-Infrared Imaging Fabry Pérot Interferometer (FIFI – Poglitsch et al. 1991) on the NASA Kuiper Airborne Observatory (KAO) in March 1993. FIFI had a $5 \times 5$ focal plane array with a detector spacing of 40″ and a *FWHM* beamsize of 55″ at the frequency of the [C II] line. The beamsize is approximately Gaussian with an equivalent disk of 69″ and a corresponding beam solid angle of $8.3 \times 10^{-8}$ sr. At the frequency of the [O I] 63 $\mu$m line, the *FWHM* beamsize is 22″. The bandpass of the Fabry-Pérot was centered at the velocity −30 km s$^{-1}$. The Lorentzian instrument profile has a spectral resolution of 64 km s$^{-1}$ for the [O I] line and 52 km s$^{-1}$ for the [C II] line, leaving both lines unresolved. Observations were performed in a beam-switching mode with a chopping frequency of 23 Hz.

The corresponding reference positions were selected from IRAS maps and expected to be free from contaminating [C II] and [O I] line emission. However, because the Carina region lies in the galactic plane, the self-chopping is still estimated to be 10−15% of the peak values. Typical integration times were 5 min per array placement.

The [C II] 158 $\mu$m map covers a region of $13 \times 11$ arcmin$^2$ and includes both Tr 14 and a large part of the molecular cloud around the western dust lane (see Fig. 1). A pointing grid of 40″ was used with additional pointings on a grid of 20″ near the center (see Fig. 2). The chopping parameters were 7′ north–south and 12′ east–west. The [O I] 63 $\mu$m map is centered on the peak [C II] emission and corresponds to an area of 12 arcmin$^2$ (see Fig. 2). Observations were made on a pointing grid of 20″ with the chopping set to 10′ east–west. Additional observations of [O I] $^3P_0-^3P_1$ 145 $\mu$m were obtained but with insufficient signal-to-noise to produce a final map. Data were calibrated by observing an internal black body source and the calibration uncertainty is estimated to be 30%. The integrated line intensities were determined from Lorentzian fits to the instrumental profile and were corrected for leakage. Pointing uncertainties are below 15″.

### 2.2. ISO observations

Low resolution grating spectra from 43 to 196 $\mu$m were obtained with the Infrared Space Observatory (ISO) using the LWS AOT 01 mode (Clegg et al. 1996). The flux and wavelength were calibrated according to the procedures described in Swinyard et al. (1996). Each spectrum consists of six fast grating scans with 0.5 s integration at each commanded grating position and ten overlapping sub-spectra, one for each of the ten detectors. The observations were sampled at 1/4 of a spectral resolution element, the latter being 0.283 $\mu$m in second spectral order (detectors SW1–SW5 covering 43−93 $\mu$m) and 0.584 $\mu$m in first spectral order (detectors LW1–LW5 covering 84−196 $\mu$m).

The Tr 14 region was observed with the LWS in a $5 \times 3$ raster centered on RA(J2000) = $10^h43^m20^s$, Dec(J2000) = $-59°34'28.4''$ (see Fig. 1). The spacing between each position was 100″, slightly bigger than the size of the LWS beam which is known to vary with wavelength between 66″ and 86″ HPFW (Gry et al. 2002). We have adopted a value of 80″ for our analysis. Post-pipeline reduction and analysis were performed using the ISO Spectroscopy Analysis Package (ISAP) and included further deglitching, averaging of the individual scans for every detector, defringing and profile fitting. No scaling between the sub-spectra was applied. The accepted absolute flux error per detector is 10% (e.g., Swinyard et al. 1996; Peeters et al. 2002). At each position in the raster, the integrated intensities for the fine structure lines were measured by fitting a Gaussian profile. Note that for the [O I] 145 $\mu$m line, only the line flux measured in the detector LW4 was used, as the emission also seen in detector LW3 is strongly affected by fringes. In the case of the [O III] line, the values measured by the SW5 and LW1 detectors agree very well and we used the SW5 value.
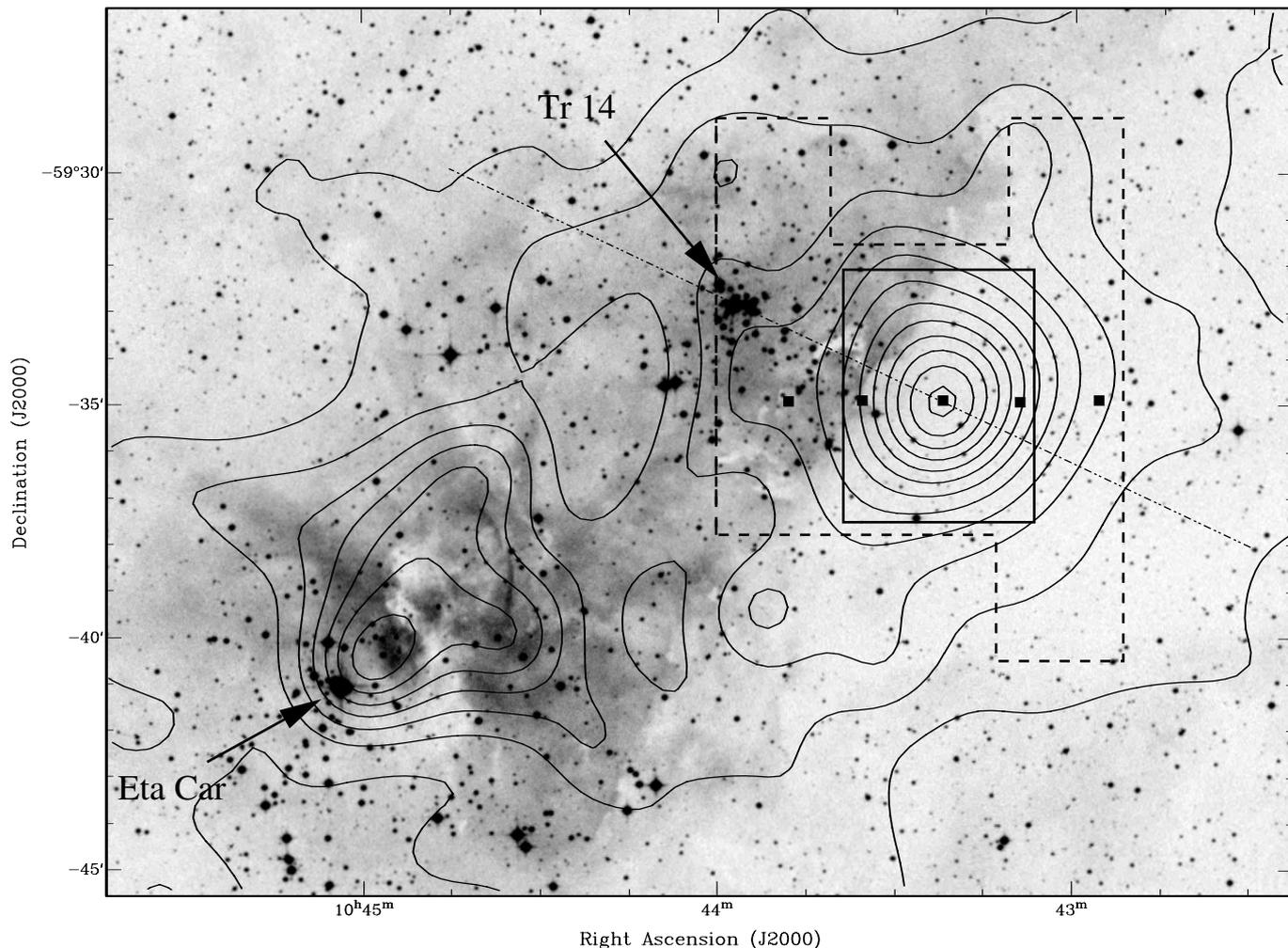
**Fig. 1.** A contour representation of IRAS 60 $\mu$m emission superimposed on an H$\alpha$ image taken from the Digitized Sky Survey. Contour levels range from 10 to 99% of the peak emission of 29 500 MJy sr$^{-1}$ in increments of 8%. The regions bounded by the respective thick dashed and solid lines indicate the extent of the [C II] 158 $\mu$m and $^{13}$CO(2−1) data discussed in this work. The thin dashed line marks the cut (joining Tr 14 to the far-infrared peak emission) used for the set of intensity-position diagrams shown in Fig. 11 and the five squares mark the positions along the central raster for the ISO observations. The centers of Tr 14 and Tr 16 (denoted by the star $\eta$ Car) are also indicated.

## 2.3. SEST observations

Observations of $^{13}$CO(2−1) were carried out with the SEST during May 1994 towards the IRAS peak adjacent to Tr 14. An area of $4 \times 5$ arcmin$^2$ was mapped using a pointing grid of 20 arcsec (see Fig. 1). Data were taken with the superseded cooled Schottky mixers and the current AOS system. An integration time of 2 min per position was adopted. Subsequent observations were obtained in 1999 August of the transitions $^{12}$CO(2−1), CS(5−4), CS(3−2) and CS(2−1). The data were taken using an on-source integration time of 1 min and a 20″ pointing grid. For the $^{12}$CO(2−1) and CS(5−4) data the IRAM-built 230-GHz SIS receiver was utilised and for the CS(3−2) and CS(2−1) data the SIS 150-GHz and 100-GHz receivers were used in parallel. The final maps cover an area of $3 \times 3$ arcmin$^2$ centered on the same position as the $^{13}$CO(2−1) map. The exception is CS(5−4) for which the final map is only $2 \times 1$ arcmin$^2$. The observing parameters for all transitions are summarized in Table 1.

**Table 1.** Observing parameters of the molecular line data. Parameters include: the transition frequency ($\nu$), the Half Power Beam Width (*HPBW*), the main beam efficiency ($\eta_{mb}$), the average system temperature ($T_{sys}$) and the average rms noise temperature per channel ($\Delta T_{rms}$).

| | $\nu$ | *HPBW* | $\eta_{mb}$ | $T_{sys}$ | $\Delta T_{rms}$ |
|---|---|---|---|---|---|
| | [GHz] | [″] | | [K] | [K] |
| **SEST 1994** | | | | | |
| $^{13}$CO(2−1) | 220.399 | 25 | 0.5 | 1250 | 0.7 |
| **SEST 1999** | | | | | |
| $^{12}$CO(2−1) | 230.537 | 24 | 0.5 | 460 | 0.4 |
| CS(5−4) | 244.935 | 21 | 0.5 | 607 | 0.4 |
| CS(3−2) | 146.969 | 34 | 0.66 | 293 | 0.2 |
| CS(2−1) | 97.980 | 52 | 0.75 | 293 | 0.2 |

For both the 1994 and 1999 data sets a position-switching operation was adopted with the position of $\eta$ Car used as the line-free off position. Zero order baselines were subtracted from all spectra. Flux calibration was done using the standard
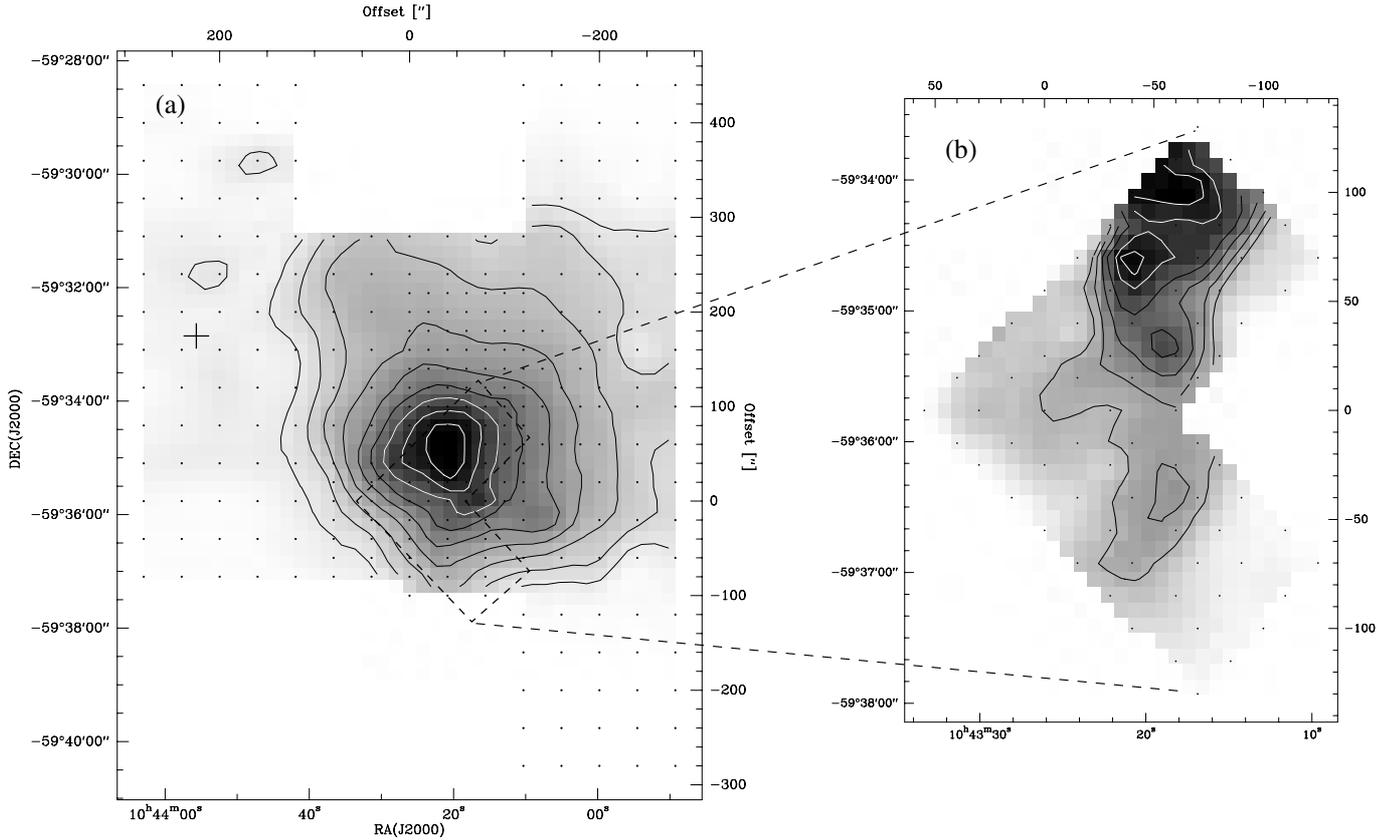
**Fig. 2.** Maps of **a)** [C II] 158 $\mu$m emission and **b)** [O I] 63 $\mu$m emission. The contour levels are 0.35 (3$\sigma$), 0.50, 0.65, 0.80, 0.95, 1.10, 1.25, 1.40, 1.56 $\times 10^{-3}$ ergs$^{-1}$ cm$^{-2}$ sr$^{-1}$ for the [C II] map, and 3.1, 3.6, 4.2, 4.8, 5.5 5.9 $\times 10^{-3}$ erg s$^{-1}$ cm$^{-2}$ sr$^{-1}$ for the [O I] map. The grid of dots represent the observed positions. Their offsets are given with respect to the position RA(J2000) = $10^h43^m26.1^s$, Dec(J2000) = $-59°35'45''$. The center of Tr 14 is marked by the cross.

chopper-wheel method. The resulting atmosphere-corrected antenna temperatures were converted to main-beam brightness temperatures utilising the values for main-beam efficiencies quoted in the SEST Handbook. The telescope pointing and subreflector focusing were checked regularly on the SiO maser in R-Car. We estimate a pointing accuracy better than 5″ and adopt the standard SEST value of 10% for the uncertainty in the antenna temperature scales. All the profiles were smoothed with a Boxcar method to a velocity resolution of 0.176 km s$^{-1}$.

## 3. Results

### 3.1. Fine-structure line emission

The maps of the emission of the fine-structure [C II] 158 $\mu$m and [O I] 63 $\mu$m lines in Tr 14 are displayed in Fig. 2. The [C II] 158 $\mu$m (hereafter [C II]) line map shows a roughly circular region of extended emission centered at RA(J2000) = $10^h43^m22^s$, Dec(J2000) = $-59°34'45''$. This matches the far-infrared dust continuum emission at 60 $\mu$m shown in Fig. 1. The [C II] peak surface brightness is 1.7 $\times 10^{-3}$ erg s$^{-1}$ cm$^{-2}$ sr$^{-1}$. The higher spatial resolution [O I] 63 $\mu$m emission is resolved into a ridge of emission running north–south with three distinct maxima. The middle peak is the brightest with a surface brightness value of 6.5 $\times 10^{-3}$ erg s$^{-1}$ cm$^{-2}$ sr$^{-1}$ and is centered

at RA(J2000) = $10^h43^m20.5^s$, Dec(J2000) = $-59°34'35''$. Detected at approximately the same position lies the peak of the [O I] 145 $\mu$m emission with a peak surface brightness of $\approx 3.2 \times 10^{-4}$ erg s$^{-1}$ cm$^{-2}$ sr$^{-1}$.

Figure 3 shows the ISO LWS spectra toward three of the central raster positions: one nearest to the H II region; one towards the peak of the [C II] emission; and one nearest to the molecular cloud. All three spectra are dominated by the dust continuum emission that peaks at 40−50 $\mu$m. Superimposed on this continuum are a series of strong fine-structure atomic lines: from the H II region – the two [O III] lines at 51.8 and 88.3 $\mu$m, [N II] at 121.7 $\mu$m, and [N III] at 57.3 $\mu$m; and from the PDR – [C II] and the two [O I] lines.

Figure 4 presents the variation of the intensities of the [C II] and the 63 and 145 $\mu$m [O I] fine-structure lines across the five ISO raster positions. Peak values for all three PDR lines were found towards the raster center (corresponding to the peak of the [C II] map): 3.3 $\times 10^{-3}$, 3.9 $\times 10^{-4}$ and 2.3 $\times 10^{-3}$ erg s$^{-1}$ cm$^{-2}$ sr$^{-1}$ for [O I] 63 $\mu$m, [O I] 145 $\mu$m and [C II] 158 $\mu$m, respectively. Values for [C II] and [O I] 145 $\mu$m emission are slightly higher (20%) than the corresponding KAO values, a difference which could be accounted for by self-chopping effects in the case of the KAO observations. For the [O I] 63 $\mu$m emission the ISO value is half that of the KAO value. This difference may be caused by beam
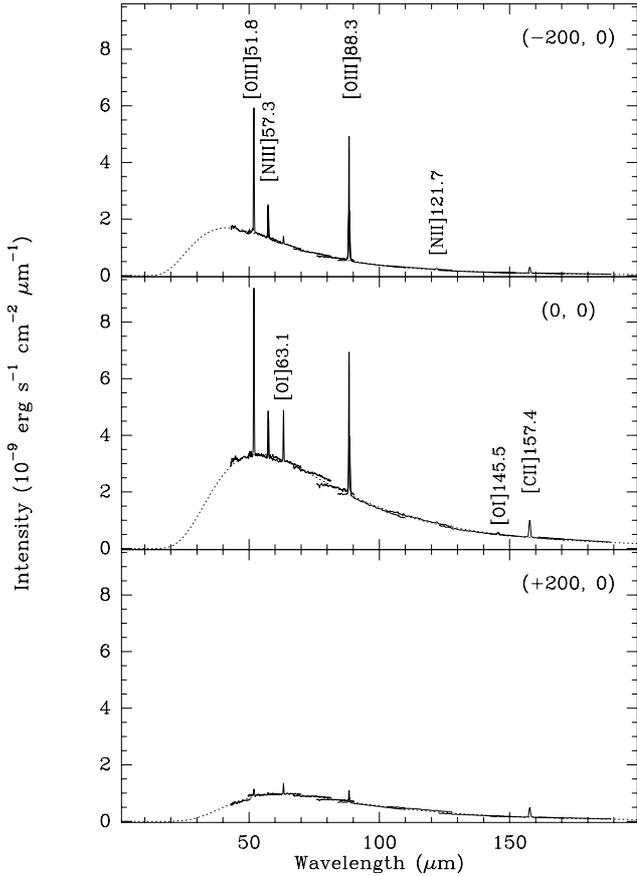
**Fig. 3.** LWS spectra (solid line) at three positions across the Tr 14 region, corresponding to the H II region (−200″, 0″), the far-infrared peak (0″, 0″) and the molecular cloud (+200″, 0″). The best-fitted modified blackbody spectra (dashed line) are shown (see text) and the fine-structure lines are identified.



**Fig. 4.** Variation of the intensity of the fine-structure lines and the dust temperature across the Tr 14 region taken from the ISO LWS observations. The location of the five data points are marked in Fig. 1 and their offsets are given with respect to the peak position (RA(J2000) = 10$^{\rm h}$43$^{\rm m}$20$^{\rm s}$, Dec(J2000) = −59°34′28.4″) along the east-west direction. **a)** The [C II] 158 μm line and the two [O I] lines at 63 and 145 μm (dashed and dotted lines, respectively). **b)** The distributions of the [O III] 88 μm line (dotted) and the dust temperature (dashed).

dilution for the ISO data. The fluxes of the PDR emission lines decrease almost symmetrically from the central peak out to the H II region and the molecular cloud. The [O III] emission line is strongest towards the H II region, which is to be expected since it arises from high excitation gas. After a steep decrease between offset −100″ and the center, the [O III] emission is still detected towards the molecular cloud with a surface brightness of a few $10^{-5}$ erg cm$^{-2}$ s$^{-1}$ sr$^{-1}$. This result could imply that extended ionized gas is surrounding the molecular cloud associated with Tr 14.

### 3.2. Far-Infrared continuum emission

Estimates for the dust temperatures have been derived by fitting the 43–196 μm spectrum with a modified black-body curve:

$$F_\lambda = \Omega_{\rm s} \times B_\lambda(T)(1 - {\rm e}^{-\tau_{\rm dust}}) \qquad (1)$$

where $\Omega_{\rm s}$ is the source solid angle, $B_\lambda(T)$ is the blackbody emission at temperature $T$, and $\tau_{\rm dust}$ is the optical depth. The dust opacity was assumed to have a spectral index of −1. The derived dust temperatures vary from 65 K towards the H II region to 40–50 K in the PDR and the molecular cloud, with a sharp transition at the PDR interface (see Fig. 4b).
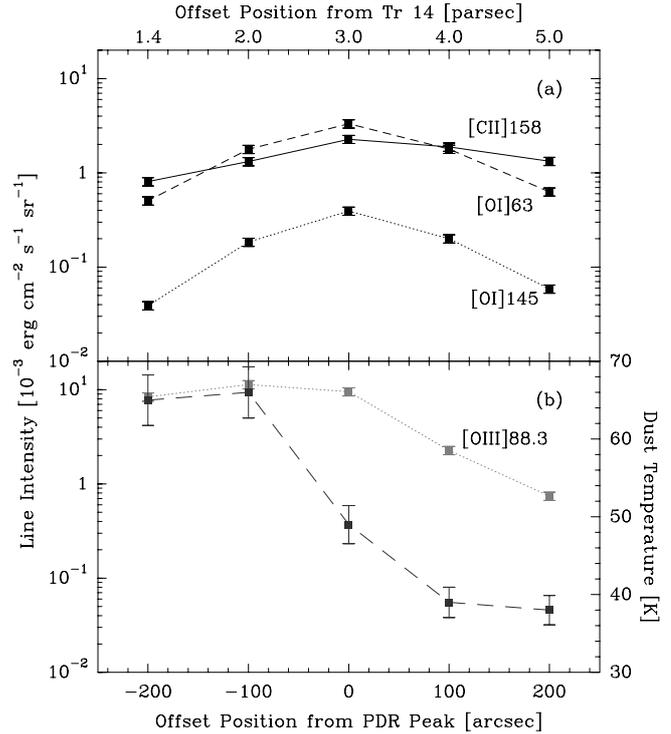
The total far-infared flux towards the KAO [C II] peak has been calculated by way of integrating the fitted blackbody curve from 43 to 196 μm (LWS range), yielding 1.2 erg s$^{-1}$ cm$^{-2}$ sr$^{-1}$. This corresponds to a total infrared luminosity of $3.5 \times 10^4 L_\odot$, which is in agreement with the estimate by Ghosh et al. (1988) but much lower than the luminosity derived by Harvey et al. (1979). The [O I] 63 μm, [O I] 145 μm and [C II] 158 μm emission lines are expected to be the dominant cooling lines. Therefore by taking the ratio of the sum of the intensity of the three lines to the total far-infrared flux, we have an estimate of the grain photoelectric heating efficiency $\epsilon$, which is the fraction of FUV photon energy that is converted to gas heating. We derive $\epsilon \sim 5 \times 10^{-3}$, a value comparable to other galactic PDRs where $\epsilon$ is typically a few $10^{-3}$ (e.g., Vastel et al. 2002 and references therein).

### 3.3. Molecular line emission

The maps of the $^{13}$CO(2–1), $^{12}$CO(2–1) and CS(3–2) velocity integrated emissions are shown in Fig. 5. For the $^{13}$CO(2–1) emission there is a prominent ring-shaped feature comprised of several emission concentrations. The curved eastern part of this ring matches a bright optical rim at the edge of the dust lane. The region of strongest integrated intensity
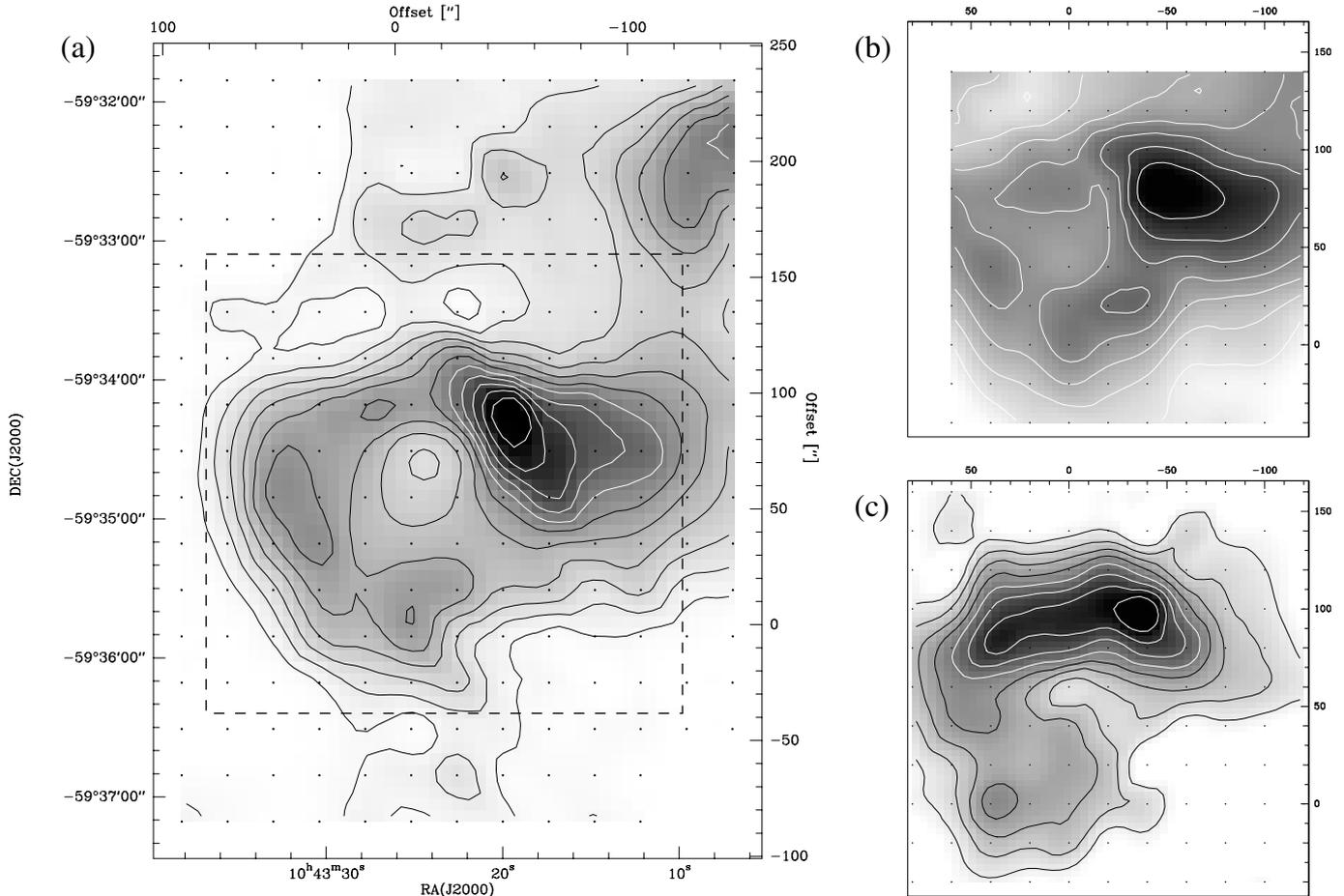
**Fig. 5.** Maps of $^{13}$CO, CO and CS emission integrated over the velocity range $-35$ to $-5$ km s$^{-1}$. The grid of dots show the observed positions, where the offsets are with respect to the reference position used in Fig. 2. The dashed box in the $^{13}$CO(2-1) map delineates the region which was subsequently mapped in $^{12}$CO(2–1) and CS(3–2). **a)** $^{13}$CO(2–1) emission with contour levels 20 ($3\sigma$), 30, 40, 50, 60, 70, 80, 90, 100, 110, 120 K km s$^{-1}$. **b)** $^{12}$CO(2–1) emission with contours from 20 to 80% of the peak emission 449 K km s$^{-1}$ in increments of 10%. **c)** CS(3–2) emission with contours from 20 to 90% of the peak emission 14 K km s$^{-1}$ in increments of 10%.

emission[1] is situated in the northwestern part of the emission ring at RA(J2000) = $10^h43^m21^s$, Dec(J2000) = $-59°34'10''$ and has a value of 126 K km s$^{-1}$. The emission ring is also traced by the $^{12}$CO(2–1) and CS emission but with some small-scale differences. Emission from the $^{12}$CO(2–1) line is clearly strongest in the northwestern part (near the peak of the $^{13}$CO(2–1) emission) whereas the brightest CS emission extends much further to the east.

A sample of individual $^{12}$CO(2–1) and $^{13}$CO(2–1) spectra are shown in Fig. 6. Both sets of profiles show a complex velocity structure with multiple components that extend over a velocity range from $-30$ to $-8$ km s$^{-1}$ and which show no signs of self absorption. There are as many as six individual velocity components in the profile towards the brightest CO integrated emission (offset position $-120$, $+60$).

The overall kinematics of the CO emitting ring are displayed in Fig. 7 as a series of velocity channel maps using the $^{13}$CO(2–1) data. In the velocity range $-25$ to $-22$ km s$^{-1}$,

the blue-shifted emission traces the western part of the ring. The velocity range $-21$ to $-19$ km s$^{-1}$ corresponds to the systemic velocity of the northern cloud ($-17$ km s$^{-1}$ as determined from the Mopra large-scale $^{12}$CO(1–0) map of Brooks et al. 1998). In this range, emission arises from the eastern part of the ring, corresponding to the region of brightest integrated CO emission. There is also another weaker emission component extending almost east–west along the northern part of the map which is likely to be part of the more extended molecular cloud. Between $-18$ and $-14$ km s$^{-1}$ there is a ridge of emission that extends in a northwest–southeast direction and which contains several emission peaks. This ridge matches the south-western part of the ring. At the most red-shifted velocities, between $-13$ and $-10$ km s$^{-1}$, the emission is detected in an isolated peak located at the eastern edge of the ring.

Figure 8 shows spectra of the CS(5–4), (3–2) and (2–1) transitions averaged over the whole map. Approximately the same four velocity components described above for the $^{13}$CO(2–1) data can be identified. The two strongest emission components are at $-25$ to $-22$ km s$^{-1}$ and $-21$ to $-18$ km s$^{-1}$. The clear detection of the CS(5–4) line in these two

---

[1] The conversion factor from K km s$^{-1}$ to erg cm$^{-2}$ s$^{-1}$ sr$^{-1}$ is: $1.569 \times 10^{-9}$ for $^{12}$CO(1–0); $1.255 \times 10^{-8}$ for $^{12}$CO(2–1); and $1.097 \times 10^{-8}$ for $^{13}$CO(2–1).
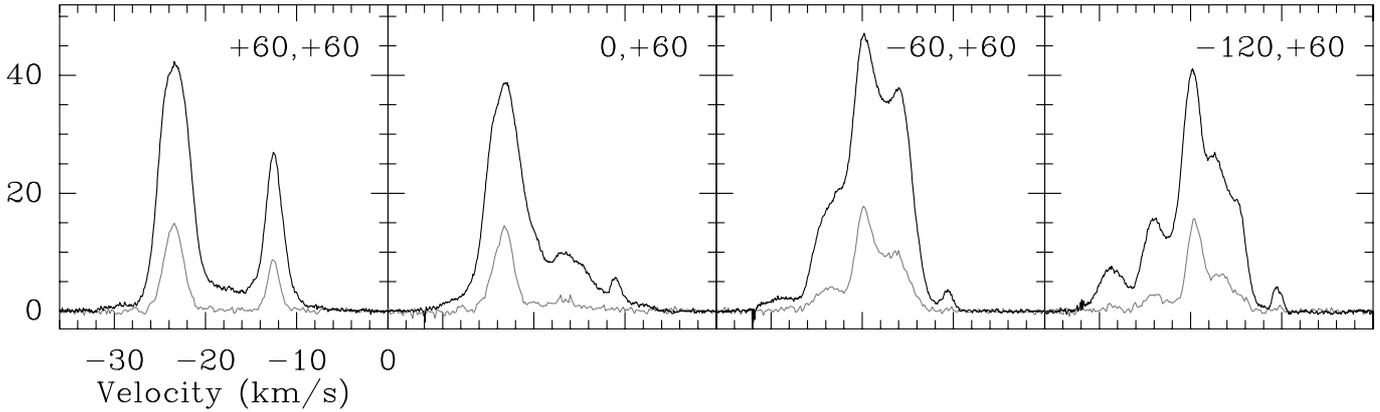
**Fig. 6.** $^{12}$CO(2–1) (solid line) and $^{13}$CO(2–1) (dashed line) spectra. The offset positions indicated in each box (in arcsec) are given with respect to the reference position used in Fig. 2.

components indicates the presence of high density ($n_{cr}(H_2) = 8 \times 10^6$ cm$^{-3}$) gas.

## 4. Discussion

Our primary goal is to determine whether the massive stellar members of Tr 14 are responsible for the observed properties of the PDR and molecular gas emission. With the new data obtained in this study it is possible to estimate the FUV radiation field associated with the PDR emission and compare it to the stellar radiation field emanating from Tr 14. The extent of the $^{13}$CO(2–1) data also allows us to study the structure and large-scale kinematics of the northern cloud.

In this section we first discuss the connection between the PDR emission and the molecular gas and quantify the mass and small-scale structure of the GMC. We then analyze the fine-structure and molecular line data towards the PDR emission peak in order to constrain the FUV radiation field and gas density at this location. Next we introduce a series of existing data to examine the stratification at the PDR/molecular gas interface and ultimately obtain a schematic model for the Tr 14 region. We then discuss whether the stellar energy budget of Tr 14 can sustain the FUV radiation field towards the PDR emission peak as well as the large-scale geometry and kinematics of the northern cloud. Finally our findings towards Tr 14 are compared with those towards the Orion bar and 30 Dor.

### 4.1. The PDR – molecular gas connection

[C II] emission can arise from PDRs and from low-density warm ionized gas. The close correlation between the morphology of the KAO [C II] emission and the molecular gas in Tr 14 suggests that the [C II] emission predominantly originates from the PDR layers of the dense molecular components. The morphology surrounding the central [C II] emission core follows the same curved shape as the molecular emission ring (see Fig. 10). The actual [C II] emission peak matches the central emission peak in the $^{13}$CO(2–1) emission ridge evident between velocities of $-18$ and $-14$ km s$^{-1}$ (see Fig. 7). Moreover there is a striking similarity between this molecular ridge and the distribution of the KAO [O I] 63 $\mu$m emission. It is tempting

to speculate that the PDR emission may be associated with this molecular gas component. However, additional velocity information on the fine structure line emission is necessary before a link can be firmly established.

As outlined in Poglitsch et al. (1991), for the case when the [C II] emission is optically thin and the density and temperature of the gas is high enough for thermalised emission, the C II column density, $N(\text{C II})$, is related to the intensity of the [C II] 158 $\mu$m emission line, $I(\text{C II})$ via:

$$N(\text{C II}) = 6.3 \times 10^{20} \, I(\text{C II}) \text{ cm}^{-2} \qquad (2)$$

We assume that C$^+$ is the predominant mode of the gas-phase carbon in PDRs (which may not necessarily be the case, see Sect. 4.3.2). Taking the abundance ratio of C/H to be $3 \times 10^{-4}$ and using the spatially averaged KAO [C II] intensity we can therefore derive a minimum average PDR column density of hydrogen nuclei $N(\text{H}) = 1.5 \times 10^{21}$ cm$^{-2}$. Integrated over the mapped area we find a minimum hydrogen mass of $\approx 360 \, M_\odot$.

### 4.2. The mass and clump-mass distribution of the molecular gas

To estimate the physical properties of the four molecular gas components identified in Fig. 7 we have averaged the $^{13}$CO(2–1) and $^{12}$CO(2–1) data over the spatial extent of each component and then fitted Gaussian functions to the resultant spectral profiles, within the matching velocity range. Table 2 lists the physical properties derived from these fits assuming local thermodynamic equilibrium (LTE). The $^{12}$CO(2–1) emission was supposed to be optically thick (and therefore equal to the gas kinetic temperature) and the $^{13}$CO(2–1) emission optically thin. Estimates of the H$_2$ column densities, $N(\text{H}_2)$, were obtained by assuming that the integrated $^{13}$CO emission is proportional to the H$_2$ column density (cm$^{-2}$) with a factor of $4 \times 10^5$ (K km s$^{-1}$)$^{-1}$ as determined by Lada et al. (1994). It is well known that this factor changes from cloud to cloud. The uncertainty value for a given type of cloud (e.g. GMC in the inner Galaxy) is about 1.5. (For further discussion see Maloney & Black 1988 and Hayakawa et al. 1999.) LTE mass estimates were determined using $M_{\text{LTE}}[M_\odot] = 6.6 \times 10^{-24} N(\text{H}_2) D^2 A$ with the distance of the cloud $D$ in parsecs and the angular
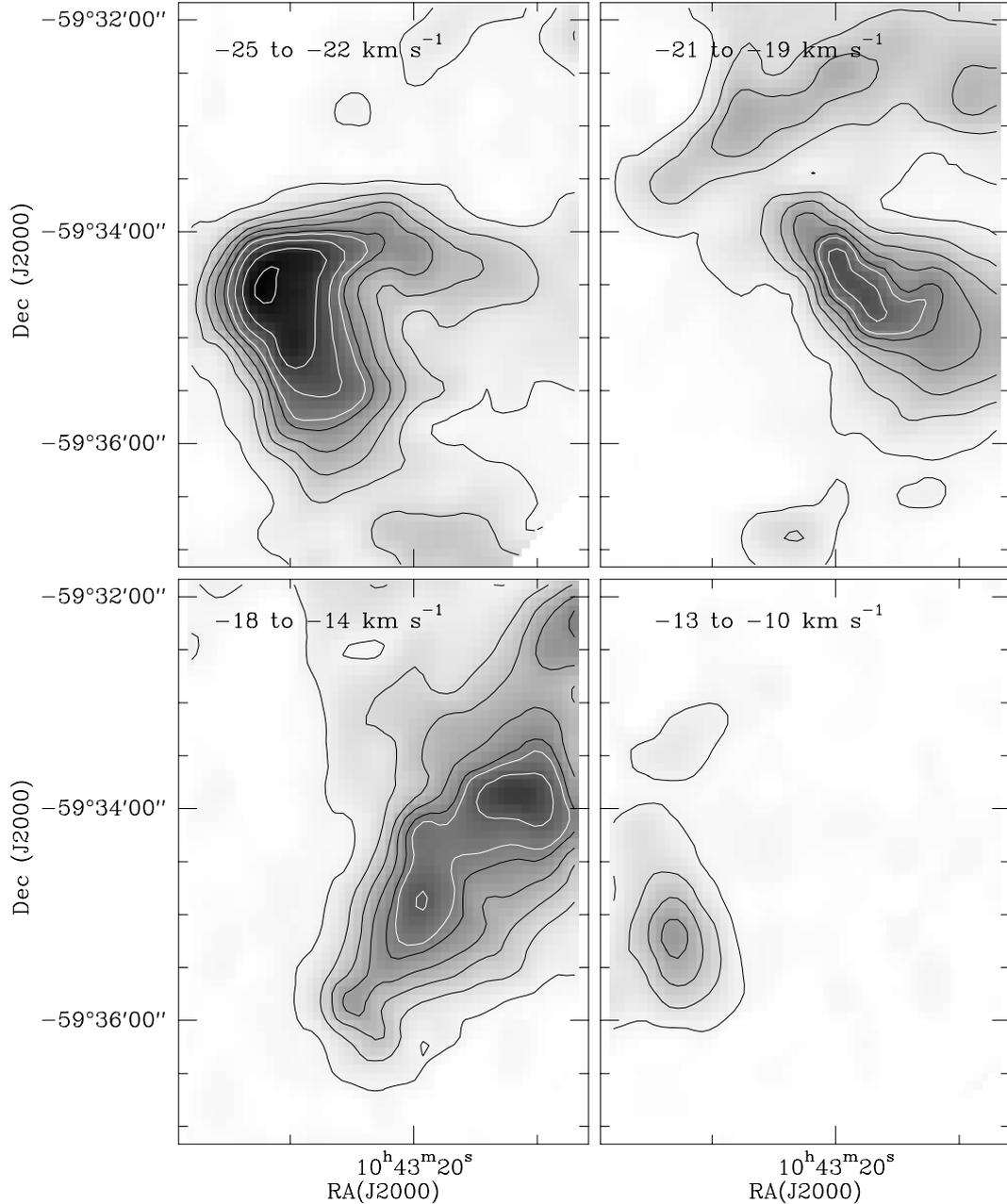
**Fig. 7.** Channel maps of the $^{13}$CO(2–1) emission integrated over 4 velocity ranges indicated in the upper left corners of each panel. The contour levels are 3 ($3\sigma$), 9, 15, 21, 27, 33, 39, 45, 51 K km s$^{-1}$.

extent $A$ in degrees. Estimates for the Virial mass were calculated using the linewidths of the $^{13}$CO(2–1) profiles, $\Delta V$ (km s$^{-1}$), and assuming a Gaussian density and velocity profile: $M_{\mathrm{vir}} = 1145 \Delta V A^{0.5} D$. Estimates for the average H$_2$ density were derived by assuming a radial density distribution.

The resulting mean H$_2$ densities ($\approx 10^3$ cm$^{-3}$) and mass range (40 to 500 $M_\odot$) are typical of warm clumps found in other GMCs (e.g. Turner 1996). In the case of two components the LTE masses are not too different from their corresponding Virial masses, suggesting that these components may be gravitationally bound.

In order to quantify the small scale structure of the molecular cloud, we applied the automated clump identification algorithm GAUSSCLUMPS to the $^{13}$CO(2–1) data cube. This

algorithm, developed by Stutzki & Güsten (1990), decomposes the data cube into a number of clumps by fitting a series of Gaussian components in an iterative process (see Kramer et al. 1998 for further details). Clumps with parameters intrinsically larger than 10% of the spatial and velocity resolution were used. Based on a $3\sigma$ noise detection, the minimum detectable clump mass is 0.07 $M_\odot$.

A total of 282 clumps were found with LTE masses ranging from 0.2 to 396 $M_\odot$, adding to a total mass of $2 \times 10^4 M_\odot$. Six of these clumps are found to be more massive than 40 $M_\odot$, contributing to over half of the total mass. The clump diameters (*FWHM*) are typically 1′ and their average H$_2$ densities lie in the range 1.5 to 5.6 $\times 10^3$ cm$^{-3}$. The clump-mass distribution (shown in Fig. 9) indicates that for clumps more massive
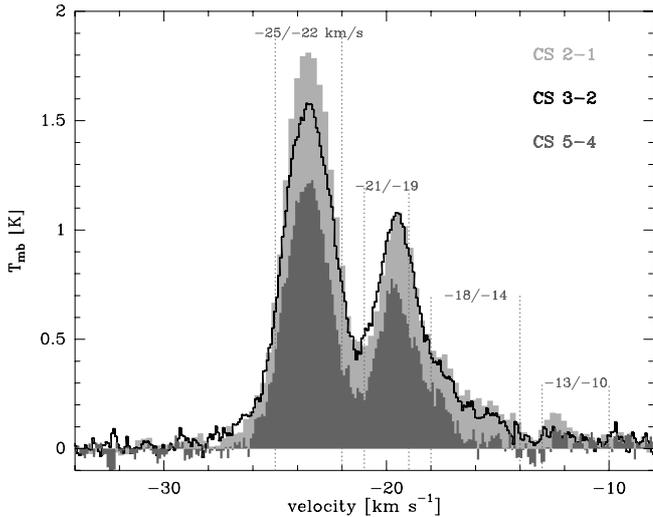
**Fig. 8.** CS(5–4), (3–2) and (2–1) spectra averaged over the whole map. The four main velocity intervals determined by the CO observations are indicated.
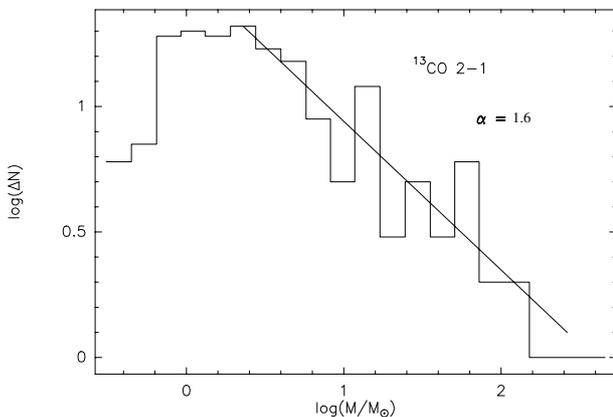


**Fig. 9.** LTE clump-mass distribution for 282 clumps found by the clump-finding algorithm GAUSSCLUMPS. $N$ is the number of clumps in each mass bin.

than 1.24 $M_\odot$, the clump-mass index is $\alpha = 1.6$, a value consistent with what has been derived in other giant molecular clouds (e.g. Kramer et al. 1998; Schneider et al. 1998).

### 4.3. Parameters at the PDR emission peak

#### 4.3.1. Application of a one-dimensional PDR model

We have compared our observed line intensities at the position of the [C II] emission peak with predictions from the stationary PDR model of Kaufman et al. (1999) in order to constrain the gas density and the FUV radiation field at the PDR surface ($A_v \leq 2$). The PDR model assumes a 1-dimensional slab exposed to an incident radiation field with a face-on geometry. The standard model parameters are given in Table 1 of Kaufman et al. (1999). Included as inputs to the model were the measured ISO fluxes for the [O I] 63 $\mu$m, [O I] 146 $\mu$m and [C II] 158 $\mu$m emission lines as well as the intensity ratio of $^{12}CO(2–1)$ and (1–0) emission derived from our $^{12}CO(2–1)$ data and the $^{12}CO(1–0)$ data presented in

Brooks et al. (1998). The CO emission was taken over the velocity range $-35$ to $-5$ km s$^{-1}$.

In the case of the Tr 14 region, the geometry of the dust lane implies more of an edge-on situation which can cause a limb-brightening effect for the optically thin [C II] and [O I] 145 $\mu$m lines. To correct for a nominal viewing angle of 60° instead of face-on, a limb-brightening factor of two has been assumed for both of these lines (calculations have been made using half the observed intensities values). The initial result did not define a unique solution and the [C II] emission line intensity appears too high. This could be caused by a contribution from non-PDR emission. Using the flux of the ISO [C II] emission toward the Tr 14 H II region (position $-200$ in Fig. 4), we estimate the non-PDR contribution to be $\approx 30\%$. Reducing the input [C II] emission accordingly leads to a better final solution defining a parameter space with a range in density of $4 \times 10^3$ to $3 \times 10^4$ cm$^{-3}$ and a range in FUV field of $6 \times 10^2$ to $1 \times 10^4$ $G_0$.

In order to obtain a second estimate of the FUV field, we determined the dust color temperature derived from the IRAS 60 $\mu$m to 100 $\mu$m flux ratio and applied it to the original PDR model of Hollenbach et al. (1991). The ratio of the two IRAS fluxes at the [C II] emission peak is $\approx 1$ which implies a dust color temperature of 50 K and a FUV flux of $10^4$ $G_\circ$.

These results should only be taken only as a first estimate in quantifying the excitation conditions within the Tr 14 PDR and a more thorough analysis incorporating other models (e.g. Le Bourlot et al. 1993) should be carried out in the future. For instance, the single-slab PDR models used here oversimplify the complex morphology of the region. The multiple components evident in the molecular line profiles and the results of the clump-mass analysis imply that a more realistic model would be one with several PDR surfaces in a clumpy molecular medium. Moreover, there are uncertainties within the PDR models themselves, particularly the charge exchange rates and the metalicity parameters (refer to Kaufman et al. 1999 for further discussion). It also should be noted that we have used a stationary model whereas the Tr 14 PDR interaction is most certainly not stationary. However, as discussed in Sect. 4.7, Tr 14 is more evolved than other well-studied Galactic PDR regions. Therefore, the interaction zones at the Tr 14 PDR interface are closer to pressure equilibrium, increasing the applicability of a stationary PDR model.

#### 4.3.2. The amount of carbon in the main phases C$^+$,C$^\circ$,CO

From the observed [C II] and $^{13}CO$ column densities and using the value for the [C I] column density given in Zhang et al. (2001) we can determine the particle numbers and therefore the fractional abundance of carbon in each of the three main carbon phases (C$^+$:C$^\circ$:CO) at the PDR emission peak. Within a 3.5′ beam Zhang et al. (2001) found a [C I] column density of $1.4 \times 10^{17}$ cm$^{-2}$. In the same area ($\approx 4$ pc$^2$), we obtain a [C II] column density of $5.9 \times 10^{17}$ cm$^{-2}$. The mean $^{13}CO$ column density of the molecular gas integrated from $-35$ to $-5$ km s$^{-1}$ is $3.5 \times 10^{16}$ cm$^{-2}$. Assuming a $^{12}CO/^{13}CO$

ratio of 50, we then obtain in a slightly smaller area ($\sim$3 pc$^2$) a CO column density of $1.7 \times 10^{18}$ cm$^{-2}$. This means the ratio C$^+$:C$^\circ$:CO is 28:7:64 indicating that the majority of gas-phase carbon is locked in CO. Several galactic PDRs with weaker [C II] emission show a ratio of around 40:20:40 (e.g. NGC 2024 Jaffe & Plume 1995; and IC 63 Jansen et al. 1996). For S106 the ratio is 10:5:85 (Schneider et al. 2003).

### 4.3.3. Application of multi-line CS analysis

A more sophisticated approach to determine the physical parameters of the molecular gas is to solve the radiative transfer equation explicitly but using the approximation that the level populations are independent of the position in the cloud. Here we use the escape probability model of Stutzki & Winnewisser (1995) for a homogeneous, spherical cloud. Analysis was performed at the PDR emission peak only and on the two brightest CS emission components for which there were clear detections of the CS(5–4) emission line: −25 to −22 km s$^{-1}$ and −21 to −18 km s$^{-1}$. We used the observed line ratio of CS(3–2) to CS(2–1) as well as the CS(5-4) line intensity. Data were smoothed to an angular resolution of 50″.

For both emission components, kinetic temperatures above 30 K were necessary for the model to converge. The outputs were in the range $10^5$ to $10^6$ cm$^{-3}$ for $n(H_2)$. We can obtain an estimate for the volume filling factor using $F_v = n_{av}/n_{local}$. In this case the local density, $n_{local}$, is obtained from the model output and the average density, $n_{av}$, is taken to be the densities listed in Table 2. The result is of the order of 1% or less for both components. Average filling factors derived from CS data of less than 5% have been reported in several other massive star-forming regions (e.g., Beuther et al. 2000; Goldsmith et al. 1997) and are consistent with small-scale structure.

The emergent scenario therefore is that the CS emission of the two most negative velocity molecular-gas components at the PDR emission peak arise from small, high density molecular clumps heated to temperatures greater than 30 K. The high densities are not in contradiction to the results from the PDR model obtained in Sect. 4.3.1 which utilised emission from a wider velocity range. Moreover, the peak PDR emission may not actually be associated with the two most negative velocity components. As already mentioned, the morphology of the PDR emission matches very well with the molecular component between velocities of −18 to −14 km s$^{-1}$, for which there is insufficient CS(5–4) emission to be included in the CS analysis.

### 4.4. Disentangling the discrete emission zones in Tr 14

The distributions of the $^{13}$CO(2–1) and KAO [C II] emission with respect to the location of Tr 14 and the dust lane are consistent with an ionizing-cluster / PDR / molecular-cloud interface, viewed approximately edge on. Further comparisons with other emission species allow us to trace the different layers within this interface.

Figure 10 shows MSX data (see Price 1995) of the Tr 14 region arising from two bands: 6.8−10.8 $\mu$m (8 $\mu$m) and 18.2−25.1 $\mu$m (20 $\mu$m) . The 8 $\mu$m band is dominated by line emission arising from PAHs which are readily associated with PDRs. The 20 $\mu$m band is dominated by continuum emission from heated dust. The 8 $\mu$m emission exhibits a bright arc centered on the detected [C II] emission peak. This arc has been traced via 3.29 $\mu$m PAH emission (Rathborne et al. 2002) and matches exactly our detected [O I] 63 $\mu$m emission ridge. It is also adjacent to the sharply curved western edge of the 4.8-GHz continuum emission arising from ionized gas (Brooks et al. 2001). This emission edge is known as Car I-W and is centered at a velocity of −25 km s$^{-1}$. Bright emission in the corresponding 20 $\mu$m image is situated closer to the Tr 14 cluster center and arises from two main components. One of these overlaps with the eastern edge of the detected [C II] emission, a second 3.29 $\mu$m PAH emission ridge, as well as a second 4.8-GHz continuum emission component known as Car I-E, with a velocity of −19 km s$^{-1}$.

To further illustrate the discrete emission zones we have taken a cut through the center of the Tr 14 cluster and the [C II] emission peak and recorded the intensity variation for a sequence of different emission tracers (see Fig. 11). One of the datasets is that of [C I] 492 GHz emission taken from the study by Zhang et al. (2001). According to models by Hollenbach & Tielens (1999), much of the [C II] and [O I] fine structure emission originates from the outermost surfaces of the PDRs whereas the [C I] fine structure emission arises from layers further within. Evident in Fig. 11 are the two emission peaks arising from 4.8-GHz continuum, 3.29 $\mu$m PAH and $^{13}$CO(2–1) emission, consistent with two PDRs separated by $\approx$1′. The brightest 3.29 $\mu$m PAH emission peak corresponds to the Car I-W continuum emission component and with the $^{13}$CO(2–1) emission arising from the velocity range −21 to −14 km s$^{-1}$. The angular resolution of both the [C I] and [CII] data is not sufficient to resolve both PDR peaks. However, in the direction away from Tr 14 is first the 4.8-GHz continuum emission peak (Car I-W), followed by the [C II] emission peak and then the [C I] emission peak.

Also evident in the sequence of cuts is a striking positional offset between the IRAS emission at 100 and 60 $\mu$m and the IRAS emission at 25 and 12 $\mu$m. The emission peak at longer wavelengths is centered on the [C II] emission peak, whereas the emission peak at shorter wavelengths (analogous to the MSX 20 $\mu$m emission) is located further towards the center of Tr 14. This positional offset has been noted in earlier studies. Cox (1995) attributes it to a strong dust temperature gradient in the direction of Tr 14.

### 4.5. Origin of the excitation of the PDR

Based on the stellar properties of Tr 14 (see Appendix A) the flux of the FUV field impinging on the position of the [C II] emission peak is estimated to be $\sim$$1.4 \times 10^4$ $G_0$ (neglecting dust effects). Moreover, using Eq. (11) of Garay & Lizano (1999), the total luminosity of Tr 14 is sufficient to heat the dust at the [C II] emission peak to $\approx$50 K. These values are consistent with the output of the PDR model analysis in Sect. 4.3.1 and implies that the massive stellar members of Tr 14 are
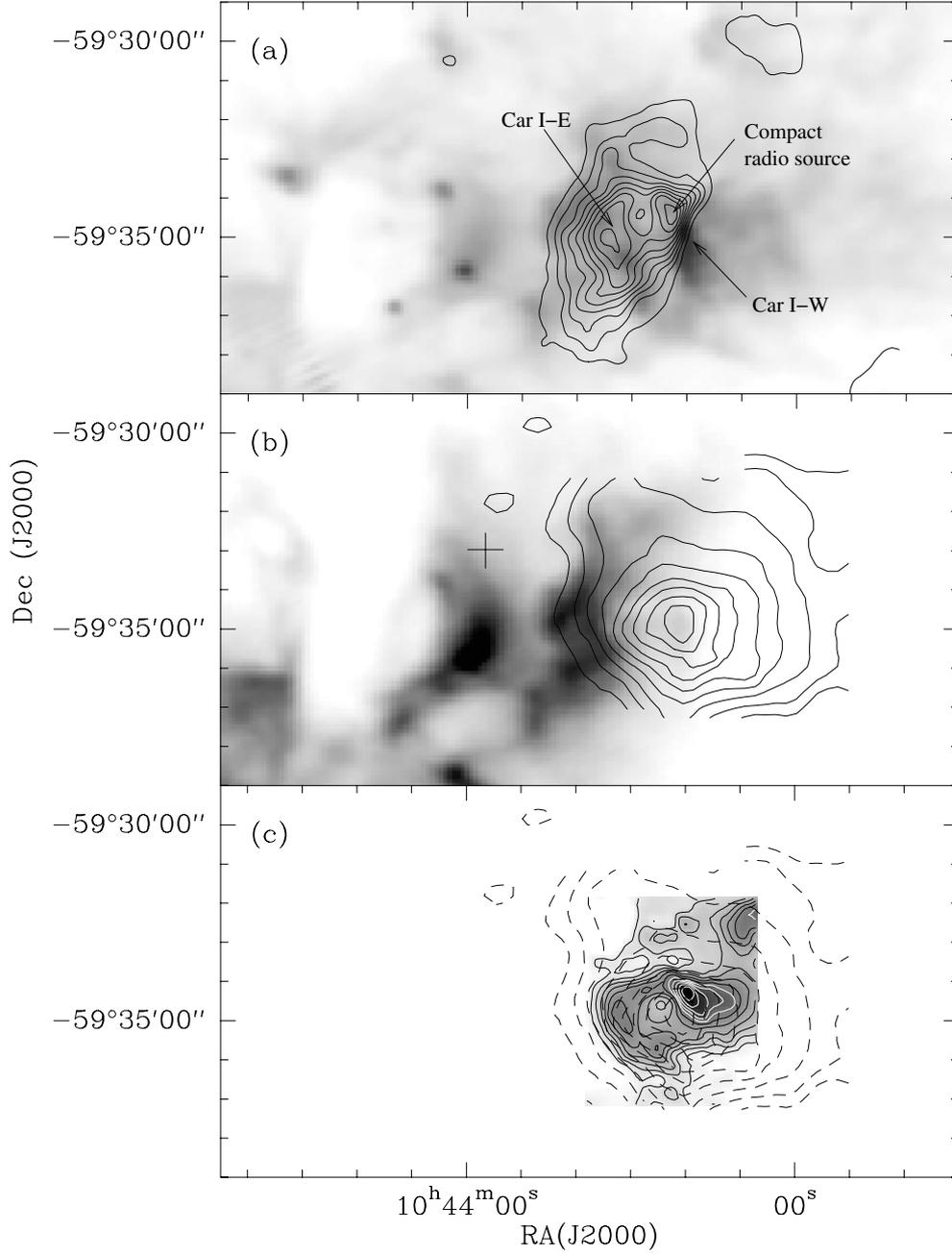
**Fig. 10.** Comparison of different emission tracers in the Tr 14 region. **a)** MSX 8 $\mu$m emission with contours of the 4.8-GHz radio continuum emission taken from Brooks et al. (2001). The contour levels are 0.08, 0.15, 0.2, 0.25, 0.3, 0.35, 0.4, 0.45, 0.5, 0.55, 0.6, 0.65 Jy beam$^{-1}$. **b)** MSX 20 $\mu$m emission with contours of the KAO [C II] 158 $\mu$m emission taken from Fig. 2. **c)** $^{13}$CO(2–1) emission taken from Fig. 5 with contours of the KAO [C II] 158 $\mu$m emission.The center of Tr 14 is marked by the cross.

**Table 2.** Derived parameters for the four components shown in Fig. 7. The parameters include mean values for the excitation temperature ($\overline{T}_{ex}$); the $^{13}$CO(2–1) optical depth ($\overline{\tau}_{^{13}CO}$); and the $^{13}$CO and H$_2$ column densities ($\overline{N}(^{13}CO)$, $\overline{N}(H_2)$, respectively). Also listed are the corresponding estimates for the LTE mass ($M_{LTE}$), Virial mass ($M_{vir}$) and average H$_2$ volume density ($\overline{n}_{H_2}$)

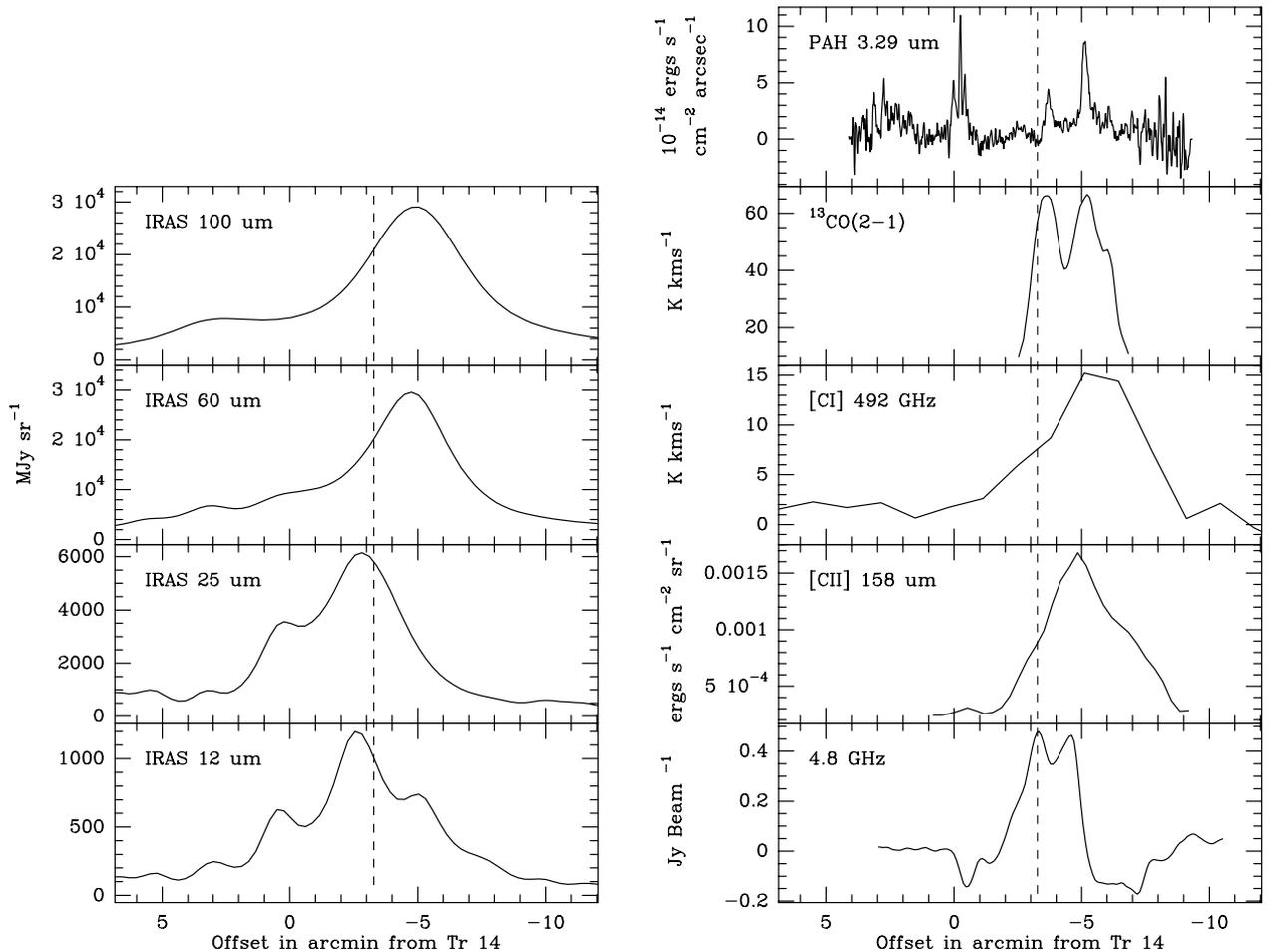| | $\overline{T}_{ex}$ | $\overline{\tau}_{^{13}CO}$ | Area | $\overline{N}(^{13}CO)$ | $\overline{N}(H_2)$ | $M_{LTE}$ | $M_{vir}$ | $\overline{n}_{H_2}$ |
|---|---|---|---|---|---|---|---|---|
| | (K) | | (degrees$^2$) | (cm$^{-2}$) | (cm$^{-2}$) | ($M_\odot$) | ($M_\odot$) | (cm$^{-3}$) |
| (a) $-25$ to $-22$ km s$^{-1}$ | 30 | 0.45 | $2.1 \times 10^{-3}$ | $2.0 \times 10^{16}$ | $8.4 \times 10^{21}$ | 540 | 420 | $1.5 \times 10^3$ |
| (b) $-21$ to $-19$ km s$^{-1}$ | 31 | 0.49 | $1.3 \times 10^{-3}$ | $1.5 \times 10^{16}$ | $6.5 \times 10^{21}$ | 260 | 1300 | $1.5 \times 10^3$ |
| (c) $-18$ to $-14$ km s$^{-1}$ | 29 | 0.27 | $1.7 \times 10^{-3}$ | $1.5 \times 10^{16}$ | $6.5 \times 10^{21}$ | 310 | 380 | $1.1 \times 10^3$ |
| (d) $-13$ to $-10$ km s$^{-1}$ | 17 | 0.2 | $0.5 \times 10^{-3}$ | $0.6 \times 10^{16}$ | $2.7 \times 10^{21}$ | 40 | 540 | $0.2 \times 10^3$ |

**Fig. 11.** Emission brightness as a function of position along the cut shown in Fig. 1. The position units are in arcmin (1 arcmin = 0.65 pc at a distance of 2.2 kpc) with respect to the center of Tr 14. [C I] 492 GHz data has been taken from Zhang et al. (2000), 4.8-GHz data from Brooks et al. (2001) and PAH 3.29 $\mu$m data from Rathborne et al. (2002). Note the PAH 3.29 $\mu$m data contains stellar (continuum) emission. The dashed vertical line marks the boundary of the dust lane.

responsible for the excitation of the PDR. This is further supported by the distribution of the [C II] emission: the [C II] emission peak is adjacent to Car I-W and the more diffuse emission at the outer eastern edge is adjacent to Car I-E. Brooks et al. (2001) have argued that Car I-E and Car I-W are two ionization fronts arising from Tr 14 and which envelope dense molecular components. Adopting this premise, the [C II] emission we have detected therefore arises from the PDRs at the interfaces of these two ionization fronts.

While Tr 14 may be the primary source of excitation for the fine structure line emission detected in this work, we cannot rule out secondary contributors. For instance, Tapia et al. (2003) have recently detected an embedded stellar population which includes at least on O9-B0 star that is associated with a compact radio continuum source (marked in Fig. 10). Furthermore, the massive stellar members of Tr 16, including $\eta$ Car, may be as close as 8 pc away.

### 4.6. Geometry of the northern molecular cloud

The large-scale $^{12}$CO(1–0) survey obtained with the Mopra Telescope (Brooks et al. 1998) illustrates that emission between

$-20$ and $-5$ km s$^{-1}$ (red-shifted) extends over the entire northern part of the nebula, including the western dust lane, whereas emission between $-35$ and $-20$ km s$^{-1}$ (blue-shifted) is confined to the dust lanes only. Assuming that the gas and dust are well intermixed (Dickel 1974), the red-shifted emission must arise from behind the optical nebulosity and the blue-shifted emission must arise from in front. This is consistent with the picture first used by de Graauw et al. (1981) in which the molecular gas and dust wrap around the nebula, partly obscuring the western part. Brooks et al. (2001) develop this picture further by suggesting that the ionized gas associated with Car I is expanding into the molecular cloud and carving out an ionized cavity.

There is no indication of a simple expanding molecular gas structure in our $^{13}$CO(2–1) data. However, as previously mentioned, the spectra do indicate a wide velocity dispersion. The highest velocity dispersion is found closest to the edge of the dust lane (and Tr 14). This corresponds to the emission component between velocities of $-25$ to $-22$ km s$^{-1}$. The coincidence of this emission distribution with a bright rim at the edge of the dust lane is consistent with it being part of the front face of the molecular cloud. Moreover, the way in which the
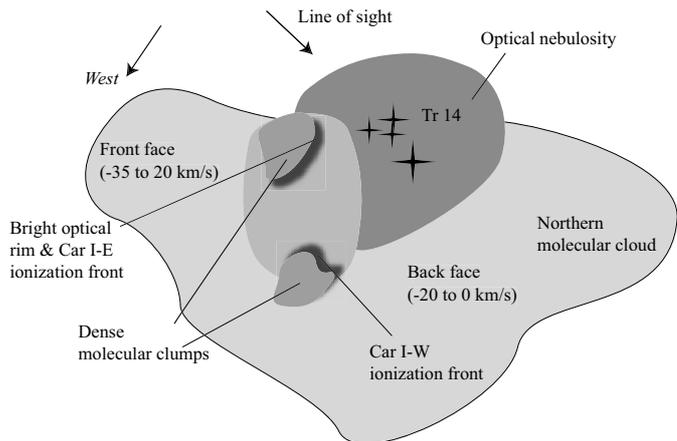
**Fig. 12.** Schematic representation of the Tr 14 region based on the data discussed in this paper.

ionization front Car I-E curves around this clump implies that it too is situated in the front part of the nebula. In contrast, Car I-W is situated well into the dust lane and is therefore enveloping molecular gas closer to the back face of the molecular cloud. Using this information we have constructed a new schematic diagram for the Tr 14 molecular cloud (see Fig. 12).

We can estimate whether the stellar winds emanating from Tr 14 can provide enough kinetic energy to sustain the measured velocity dispersion between the front and back face of the northern molecular cloud. Consider the most blue-shifted molecular component in Fig. 7 (between velocities of $-25$ to $-22$ km s$^{-1}$). Adopting a value of 6 km s$^{-1}$ for the central velocity with respect to the systemic velocity of the cloud ($-17$ km s$^{-1}$) and a total mass of 540 $M_\odot$ (see Table 2) gives a kinetic energy of $2 \times 10^{47}$ erg. The total mechanical luminosity output from the center of Tr 14 is estimated to be $6 \times 10^{45}$ erg yr$^{-1}$ (see Table A.1). The molecular component subtends a solid angle of 0.2 from the center of Tr 14. Therefore if we take the time period over which the stellar winds have been active to be $10^6$ yr (e.g. Tapia et al. 2003) then the amount of kinetic energy available to the molecular component is $9 \times 10^{49}$ erg. This implies that the stellar winds from Tr 14 can sustain the velocity dispersion measured in our molecular-line data.

### 4.7. Comparison with other PDR regions

A summary of the parameters for the Tr 14 PDR are listed in Table 3. Also included are the most prominent well-studied PDRs listed in Table 4 of Vastel et al. (2002). A value of $10^3$–$10^4$ $G_0$ for the Tr 14 FUV field is comparable to that found in 30 Dor and the reflection nebulae NGC 7023 and NGC 2068. In contrast, star-forming regions such as M17, Orion Bar and W49N all have FUV fields around $\approx 10^5$ $G_0$.

In the case of the Orion Bar, the characteristics of the O6 star, $\theta^1$ Ori C, determines most of the properties of the ionized material and the PDR (O'Dell 2001; Hollenbach & Tielens 1997). The distance between $\theta^1$ Ori C and the main ionization front is $\approx 0.25$ pc. For comparison, the distance between the Tr 14 center and the Car I-W ionization front

is $\approx 2$ pc. Moreover, the ionization front adjacent to the brightest [C II] emission in the 30 Dor is located $\approx 20$ pc northeast of the luminous star cluster R136 (Israel et al. 1996).

The greater displacement between the ionization fronts and the exciting cluster for the Tr 14 and 30 Dor regions may explain why the measured PDR FUV fields are relatively low. For the Tr 14 region the bulk of the molecular material in the vicinity of the Tr 14 cluster has been destroyed and what we are seeing now are PDRs forming at the remaining outer parts of the GMC. It appears that the expanding ionization fronts arising from the Tr1 4 cluster are responsible for both the PDR and the destruction of the molecular gas. In the case of the Orion Bar the host molecular cloud (OMC-1) appears to be still relatively intact and therefore the PDRs have formed much closer to the exciting stars.

## 5. Conclusions

We have presented a detailed view of the morphology and the physical conditions prevailing in the PDR associated with the Tr 14 stellar cluster in the Carina Nebula. Included in this study were observations taken with the KAO of the fine-structure emission lines [C II] 158 $\mu$m and [O I] 63 $\mu$m as well as selected CO and CS transitions obtained using the SEST. Also incorporated into the study were a series of existing data including *ISO* LWS full grating spectra and IRAS and *MSX* images.

The PDR emission arises from the dust lane adjacent to Tr 14 with a minimum hydrogen mass of 360 $M_\odot$. The grain photoelectric heating efficiency, $\epsilon$, is estimated to be $\approx 5 \times 10^{-3}$ with the majority of the gas-phase carbon existing as CO. Results from a 1-dimensional PDR model at the emission peak imply a FUV field of $\approx 10^4$ $G_0$ and a density of $\approx 10^4$ cm$^{-3}$. The PDR emission overlaps with the warmest and densest part of the northern molecular cloud. Here the morphology of the gas resembles a ring which can be decomposed into four main velocity components ranging from $-30$ to $-8$ km s$^{-1}$ and with average hydrogen densities of $\approx 10^3$ cm$^{-3}$ and masses in the range 40 to 540 $M_\odot$. There is evidence of a clumpy structure down to small scales with a volume-filling factor of less than 1%. Results from a multi-line CS analysis show that at the location of the PDR emission peak the two most negative velocity components have local hydrogen densities greater than $\approx 10^5$ cm$^{-3}$ and temperatures greater than 30 K.

The Tr 14 cluster, in particular the O3 star HD93129A, determines the properties of the region. The emanating radiation field is sufficient to produce the ionization fronts and the FUV flux measured at the PDR emission peak. Furthermore, the kinetic energy provided by the stellar winds can sustain the high velocity dispersion measured in the molecular gas. The overall geometry of the northern molecular cloud associated with Tr 14 is one in which the molecular gas wraps around the optical nebulosity leaving a cavity in the vicinity of the cluster. The PDR emission and ionization fronts are currently forming at the outer parts of the original GMC.

**Table 3.** A summary of the PDR parameters for Tr 14. The intensities (I) are in erg s$^{-1}$ cm$^{-2}$ sr$^{-1}$.

| Source | Distance | $I([\text{O\,I}]\,63\,\mu m)$ | $I([\text{O\,I}]\,145\,\mu m)$ | $I([\text{C\,II}]\,158\,\mu m)$ | $I(^{12}CO(1\text{-}0))$ | $I$(FIR) | Log $(G)$ | $\epsilon$ |
|---|---|---|---|---|---|---|---|---|
| | kpc | $10^{-4}$ | $10^{-4}$ | $10^{-4}$ | $10^{-7}$ | | $10^4\,G_0$ | $10^{-4}$ |
| Tr 14 | 2.2 | 33 | 3.9 | 23 | 3.9 | 1.2 | 3–4 | 50 |
| W49N | 11.4 | 31–80 | 4.6–12 | 11–28 | 4.6 | 33.5 | 5.5 | 1.4–3.6 |
| Orion Bar | 0.47 | 400 | 20 | 60 | 4 | 5 | 4.6 | 110 |
| M17 SW | 2.5 | 150 | 19 | 26 | 7 | 6.7 | 4.7 | 47 |
| 30 Doradus | 49 | 4.9 | 0.4 | 5 | 0.1 | 0.6 | 3.7 | 17 |

**Table A.1.** Parameters for the brightest stellar members of Tr 14. Values include: luminosity[a] ($L$); effective temperature[a] ($T_{\text{eff}}$); FUV luminosity[b] ($L_{\text{FUV}}$); ionizing photon flux per second[b] ($N_L$), stellar wind terminal velocity[c] ($v_\infty$); stellar wind mass-loss rate[d] ($\dot{M}$) and the mechanical luminosity ($L_W$) given by $0.5 \times \dot{M} v_\infty^2$.

| Star[a] | Spectral[a] Type | $L$ $10^5\,L_\odot$ | $T_{\text{eff}}$ $10^4$ K | $L_{\text{FUV}}$ $10^5\,L_\odot$ | $N_L$ $10^{47}$ s$^{-1}$ | $v_\infty$ km s$^{-1}$ | $\dot{M}$ $10^{-7}\,M_\odot$ yr$^{-1}$ | $L_W$ $10^{43}$ erg yr$^{-1}$ |
|---|---|---|---|---|---|---|---|---|
| HD93129A | O3I | 47.9 | 4.7 | 22.4 | 594 | 3000 | 533 | 477 |
| HD93160 | O6III | 9.1 | 4.0 | 5.5 | 90 | 2500 | 23 | 14 |
| HD93161W | O6.5V | 5.5 | 4.0 | 3.3 | 55 | 2600 | 11 | 8 |
| HD93161E | O6.5V | 10.0 | 4.3 | 4.7 | 163 | 2600 | 27 | 19 |
| HD93128 | O3V | 15.5 | 5.3 | 5.6 | 214 | 3200 | 48 | 49 |
| HD93129B | O3V | 13.5 | 5.3 | 4.9 | 186 | 3200 | 40 | 41 |
| 7 | O6.5V | 2.4 | 4.0 | 1.4 | 24 | 2600 | 3.8 | 2.6 |
| 8 | O6V | 3.9 | 4.1 | 2.3 | 35 | 2600 | 7.5 | 5.0 |
| 11 | O8V | 2.0 | 3.6 | 1.3 | 12 | 1900 | 3.6 | 1.3 |
| 13 | O9V | 0.72 | 3.3 | 0.5 | 6 | 1500 | 1.1 | 0.25 |
| 15 | O9V | 1.0 | 3.3 | 0.6 | 8 | 1500 | 1.6 | 0.36 |
| 23 | 09V | 0.22 | 3.3 | 0.7 | 2 | 1500 | 0.2 | 0.05 |
| 25 | 09V | 0.3 | 3.3 | 0.2 | 2 | 1500 | 0.3 | 0.06 |
| *Total* | | ~110 | | ~50 | ~1400 | | | ~600 |

[a] Taken from Vázquez et al. (1996).
[b] Derived using stellar models of Kurucz (1997).
[c] Taken from Table 1 in Kudritzki & Puls (2000).
[d] According to the wind-momentum luminosity relation given in Eq. (10) by Kudritzki & Puls (2000).

## Appendix A: Stellar energy budget of Tr 14

Table A.1 lists the properties of the brightest stellar members of Tr 14 quoted by Vázquez et al. (1996). Values for their luminosity and effective temperature were derived using bolometric corrections from Schmidt-Kaler (1982) and atmospheric models of Schaller et al. (1992). These 13 stars represent approximately ~50% of the total stellar luminosity and ~40% of the total mass of Tr 14. The remaining stars in the cluster are all younger than spectral type O9. Estimates for the FUV radiation field and Lyman continuum photon flux from each of the 13 stars have been derived using stellar energy distributions models of Kurucz (1997). In addition, estimates for the mechanical luminosity estimate have been obtained using stellar mass-loss rates and terminal velocities given in Kudritzki & Puls (2000).

Of the stars listed here all but 3 are concentrated within 1 arcmin of each other and centered at the core of Tr 14. This core is located ~4 arcmin to the northeast of the [C II] emission peak. The outlying stars, HD93160 and 13, are also ~4 arcmin from this position, but located further to the east. Star 23 is situated less than 2 arcmin away yet contributes relatively little to the overall flux. Therefore it is fair to assume that the bulk of the source of the radiation field and mechanical luminosity is separated by ~4 arcmin from the location of the [C II] emission peak. Assuming zero projection this translates to 2.6 pc at a distance of 2.2 kpc. Therefore the maximum value for

the FUV field impinging on the position of the [C II] emission peak is estimated to be $\sim 1.4 \times 10^4 \, G_0$ (neglecting dust effects).

# References

Beuther, H., Kramer, C., Deiss, B., & Stutzki, J. 2000, A&A, 362, 1109

Brooks, K. J., Burton, M. G., Rathborne, J. M., Ashley, M. C. B., & Storey, J. W. V. 2000, MNRAS, 319, 95

Brooks, K. J., Storey, J. W. V., & Whiteoak, J. B. 2001, MNRAS, 327, 46

Brooks, K. J., Whiteoak, J. B., & Storey, J. W. V. 1998, Proc. Astron. Soc. Aust., 15, 202

Clegg, P. E., Ade, P. A. R., Armand, C., et al. 1996, A&A, 315, L38

Cox, P. 1995, RevMexAA (Ser. Conf.), 2, 105

Cox, P., & Bronfman, L. 1995, A&A, 299, 583

Davidson, K., & Humphreys, R. M. 1997, ARA&A, 35, 1

de Graauw, T., Lidholm, S., Fitton, B., et al. 1981, A&A, 102, 257

Dickel, H. R. 1974, A&A, 31, 11

Feinstein, A. 1995, RevMexAA (Ser. Conf.), 2, 57

Garay, G., & Lizano, S. 1999, PASP, 111, 1049

Ghosh, S. K., Iyengar, K. V. K., Rengarajan, S. N., et al. 1988, ApJ, 330, 928

Goldsmith, P. F., Bergin, E. A., & Lis, D. C. 1997, ApJ, 491, 615

Grabelsky, D. A., Cohen, R. S., Bronfman, L., & Thaddeus, P. 1988, ApJ, 331, 181

Gry, C., Swinyard, B., Harwood, A., et al. 2002, in LWS – The Long Wavelength Spectrometer, ISO Handbook, ed. T. G. Millar, & J. Blommaert, Vol. 4 (LWS), SAI/99-077/Dc. (Noodwijk: ESA), 79

Habing, H. J. 1968, Bull. Astr. Inst. Netherlands, 19, 421

Harvey, P. M., Hoffmann, W. F., & Campbell, M. F. 1979, ApJ, 227, 114

Hayakawa, T., Mizuno, A., Onishi, T., et al. 1999, PASJ, 51, 919

Hillenbrand, L. A. 1997, AJ, 113, 1733

Hollenbach, D. J., Takahashi, T., & Tielens, A. G. G. M. 1991, ApJ, 377, 192

Hollenbach, D. J., & Tielens, A. G. G. M. 1997, ARA&A, 35, 179

Hollenbach, D. J., & Tielens, A. G. G. M. 1999, Rev. Mod. Phys., 71, 173

Israel, F. P., Maloney, P. R., Geis, N., et al. 1996, ApJ, 465, 738

Jaffe, D. T., & Plume, R. 1995, ASP Conf. Ser., Vol. 73

Jansen, D. J., van Dishoeck, E. F., Keene, J., Boreiko, R. T., & Betz, A. L. 1996, A&A, 309, 899

Kaufman, M. J., Wolfire, M. G., Hollenbach, D. J., & Luhman, M. L. 1999, ApJ, 527, 795

Kramer, C., Stutzki, J., Röhrig, R., & Corneliussen, U. 1998, A&A, 329, 294

Kudritzki, R.-P., & Puls, J. 2000, A&ARv, 38, 613

Kurucz, R. 1997, in Fundamental Stellar Properties (Dordrecht: Kluwer Academic Publishers), ed. T. R. Bedding, & J. J. D. Booth, Proc. IAU Colloq., 189

Lada, C. J., Lada, E. A., Clemens, D. A., & Bally, J. 1994, ApJ, 429, 694

Le Bourlot, J., Pineau des Forêts, G., Roueff, E., & Flower, D. 1993, A&A, 267, 233

Maloney, P., & Black, J. H. 1988, ApJ, 325, 389

Meixner, M., Haas, M. R., Tielens, A. G. G., Erickson, E. F., & Werner, M. 1992, ApJ, 390, 499

O'Dell, C. R. 2001, A&ARv, 39, 99

Peeters, E., Martín-Hernández, N. L., Damour, F., et al. 2002, A&A, 381, 571

Poglitsch, A., Beeman, J. W., Geiz, N., et al. 1991, in Atoms, ions and molecules: New results in spectral line astrophysics, ASP Conf. Ser., 16, 451

Price, S. D. 1995, Space Sci. Rev., 74, 81

Rathborne, J. M., Burton, M. G., Brooks, K. J., et al. 2002, MNRAS, 331, 85

Schaller, G., Schaerer, D., Meynet, G., & Maeder, A. 1992, A&AS, 96, 269

Schmidt-Kaler, T. 1982, Landolt-Bornstein, I, 2b

Schneider, N., Simon, R., Kramer, C., et al. 2003, A&A, 406, 915

Schneider, N., Stutzki, J., Winnewisser, G., & Block, D. 1998, A&A, 335, 1049

Stutzki, J., & Güsten, R. 1990, ApJ, 356, L63

Stutzki, J., & Winnewisser, G. 1995, A&A, 144, 13

Swinyard, B. M., Clegg, P. E., Ade, P. A. R., et al. 1996, A&A, 315, L43

Tapia, M., Roth, M., Vázquez, R. A., & Feinstein, A. 2003, MNRAS, 339, 44

Turner, B. E. 1996, in Astrophysical Implications of the Laboratory Study of Presolar Materila (New York: American Insitute of Physics), ed. T. J. Bernatowicz, & E. Zinner, 477

Vastel, C., Spaans, M., Ceccarelli, C., Tielens, A. G. G. M., & Caux, E. 2002, A&A, 376, 1064

Vázquez, R. A., Baume, G., Feinstein, A., & Prado, P. 1996, A&AS, 116, 75

Walborn, N. R., & Blades, J. C. 1997, ApJS, 112, 457

Wolfire, M. G., Tielens, A. G. G. M., & Hollenbach, D. J. 1990, ApJ, 358, 116

Zhang, X., Lee, Y., Bolatto, A., & Stark, A. A. 2001, ApJ, 553, 274